Review

Wiley Online Library

ELECTROANALYSIS

DOI: 10.1002/elan.202060334

Recent Progress of Single-atom Catalysts in the Electrocatalytic Reduction of Oxygen to Hydrogen Peroxide

Weiya Zhu[a, b] and Shaowei Chen*[b]

Abstract: Single-atom catalysts (SACs) have been attracting extensive interest in the electrocatalytic production of hydrogen peroxide by oxygen reduction reaction (ORR). This is due to the maximal efficiency of atom utilization and intimate interaction of the metal centers with the supporting matrix that may be exploited for deliberate manipulation of the electrocatalytic activity and selectivity, in comparison with the conventional nanoparticle counterparts. Herein, we summarize recent progress of the design and engineering of SACs towards ORR for H_2O_2 generation, based on both noble and non-noble metals. We conclude the review with a perspective highlighting the promises and challenges involved in future research.

Keywords: single-atom catalyst · oxygen reduction reaction · hydrogen peroxide · selectivity

1 Introduction

Hydrogen peroxide (H_2O_2) is listed as one of the 100 most important chemical substances in the world and has found a wide range of applications in the chemical industry, medicine, and environmental protection [1–3]. Currently, industrial H_2O_2 is prepared by the hydrogenation reaction of anthraquinone with H_2, and subsequent oxidation by O_2 in an organic medium [4–6]. This method has the following disadvantages. First, it is a multi-step process that requires a large amount of energy input and generates a lot of wastes. Second, the high concentration of H_2O_2 poses a safety hazard for transportation, due to easy decomposition and instability. By contrast, electrochemical methods have the advantages of simple reaction conditions, clean production process, and low time consumption [7]. For example, in water treatment plants and pulp mills, H_2O_2 can be in situ electrocatalytically generated for oxidative bleaching or sterilization, which is highly efficient and flexible [8].

There are currently two routes for the electrocatalytic preparation of H_2O_2, water oxidation reaction (WOR) and oxygen reduction reaction (ORR) that use water and O_2 as the reaction substrates, respectively [9–11]. In general, WOR involves rather simple experimental conditions, without the need of a gas diffusion electrode; yet it requires an ultra-high overpotential, and currently there is a lack of effective electrocatalysts with high selectivity and stability [12–15]. Therefore, electrocatalytic H_2O_2 production primarily relies on two-electron ORR [16,17].

Thus far, many materials, such as noble metals, metal alloys and carbon-based nanocomposites, have been examined as electrocatalysts for two-electron ORR [18–23]. Among these, single-atom catalysts (SACs) have emerged as a unique family of ORR catalysts due to their high mass activity and selectivity [24,25]. In SACs, the metal centers are generally embedded within a supporting matrix by coordination bonds with heteroatom dopants, where the electron transfer leads to the formation of an electrocatalytic active site [26–28]. In fact, the synergistic interaction between the metal centers and surrounding coordination atoms is the main reason for the high activity of SACs. SACs can also conveniently and flexibly manipulate the selectivity of ORR from four-electron to two-electron by a careful variation of the central atom and coordination configuration [29,30], by taking advantage of recent breakthroughs in understanding the catalytic mechanisms and reaction pathways at the atomic level. Remarkably, although SACs generally have a large surface energy, in a number of studies SACs have shown more stable physicochemical properties and longer cycle life than the conventional nanoparticle counterparts [31].

It is well-known that ORR is a multi-electron transfer process [32–35], involving two main pathways: the four-electron pathway where O_2 is reduced to H_2O (eq. 1 and 2) and the two-electron one where H_2O_2 is produced instead (eq. 3 and 4),

Four-electron pathway:

$$\text{(alkaline media)}\quad O_2 + 2H_2O + 4e^- \rightarrow 4OH^- \quad E^\circ = +0.40\,V \tag{1}$$

[a] W. Zhu
School of Materials Science and Engineering, South China University of Technology, Wushan, Guangzhou, Guangdong 510031, China
[b] W. Zhu, S. Chen
Department of Chemistry and Biochemistry, University of California, 1156 High Street, Santa Cruz, California 95064, United States
E-mail: shaowei@ucsc.edu

(acidic media)

$$O_2 + 4H^+ + 4e^- \rightarrow 2H_2O \; E^\circ = +1.23\,V \quad (2)$$

Two-electron pathway:

(alkaline media)

$$O_2 + 2H_2O + 2e^- \rightarrow H_2O_2 + 2OH^- \; E^\circ = +0.06\ V \quad (3)$$

(acidic media)

$$O_2 + 2H^+ + 2e^- \rightarrow H_2O_2 \; E^\circ = +0.70\ V \quad (4)$$

It should be noted that H_2O_2 can be produced as a reaction intermediate in the four-electron pathway. Thus, to selectively produce H_2O_2, the four-electron pathway needs to be suppressed, which can be achieved by deliberate engineering of the catalytic active centers. Electrochemical four-electron ORR involves three major intermediates, i.e., OOH*, O* and OH*, and more than three reduction steps, whereas a single adsorbed OOH* intermediate is considered for the two-electron ORR (Figure 1a) [36]. Ideally, there should be strong adsorption of O_2 molecules on the catalyst surface to induce the formation of OOH*; yet weak adsorption of OOH* is desired to facilitate the desorption from the catalyst surface to generate H_2O_2. In fact, a prolonged residence time of OOH* on the catalyst surface is not conducive to the selective production of peroxides, because dissociation of OOH* may occur (breaking of the O–O bond), which leads to the formation of O* and OH* intermediates and eventually reduction to H_2O. Therefore, the optimal catalyst should minimize the kinetic barriers of O_2 adsorption and OOH* desorption to ensure high reduction activity, while maximizing the kinetic barriers of OOH* reduction/dissociation to O* and OH*, such that high selectivity to the production of H_2O_2 can be achieved [37,38].

SACs have shown great advantages in meeting these requirements for the selective production of H_2O_2 by ORR electrocatalysis, which can be understood within the context of the interaction between the overall (or geometric) effect and the ligand (or electron) effect [39]. In ORR, oxygen can be adsorbed on the surface of the catalyst in two different ways (Figure 1b) [40]. One is dissociative side-on adsorption, which leads to an elongation of the bond length and weakening of the oxygen-oxygen double bond, generating H_2O as the final product. The other is associative end-on adsorption, where oxygen is adsorbed in the form of OOH*, facilitating the formation of H_2O_2. Note that on bulk catalyst surfaces [41], the OOH* and O* intermediates can adsorb onto the top and hollow positions, respectively. By contrast, for SACs, only the top sites are available for adsorption due to the atomic isolation of the active sites. That is, the lack of hollow sites on the surface of SACs renders it unlikely to produce O* intermediates, such that OOH* is selectively produced. This suggests that SACs are inherently advantageous for two-electron ORR [42].

In fact, a large number of theoretical and experimental studies have shown that the catalytic activity and selectivity of H_2O_2 production are mainly determined by the binding free energy of OOH* (ΔG_{OOH*}) [31,43,44]. In density functional theory (DFT) calculations [45], a constant difference of 3.2 ± 0.2 eV is found between the binding free energies of OOH* and OH*, and the binding free energy of OH* (ΔG_{OH*}) is also used as a descriptor of the two-electron ORR [46]. In a recent study, Guo et al. [36] carried out DFT calculations to study the feasibility of using SACs towards two-electron ORR. They constructed a total of 210 SAC models, of which metal elements covered both noble metals such as Pt and Pd and non-noble metals like Fe and Co (Figure 1c). The non-metallic anchoring substrates coordinated with the metal atoms include graphene with various defects and macrocyclic complex substrates, such as porphyrin and phthalocyanine [47–49]. Of these, 31 SACs were found to not only enhance the adsorption of OOH*, but also inhibit the adsorption of O*, and are considered to be viable for highly selective production of H_2O_2. The ΔG_{OOH*} calculated for the SACs shows a volcano variation

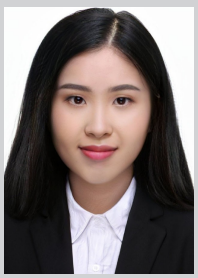

Weiya Zhu received her B.S. degree in Inorganic Materials in 2015 from Shandong University, China, and then went on to South China university of Technology to pursue a Ph.D. degree in Materials. In 2019, with the support of a research fellowship from the China Scholarship Council, she came to the University of California Santa Cruz (UCSC) as a visiting student to conduct electrochemical research under the supervision of Professor Shaowei Chen. Her research interests include surface functionalization of nanoparticles and single atom catalysts for electrochemical energy technologies.

Shaowei Chen finished his undergraduate studies in China in 1991 with a B.S. degree in Chemistry from the University of Science and Technology of China, and then went to Cornell University receiving his M.S. and Ph. D. degrees in 1993 and 1996 respectively. Following a postdoctoral appointment in the University of North Carolina at Chapel Hill, he started his independent career in Southern Illinois University in 1998. In summer 2004, he moved to the University of California at Santa Cruz. He is currently a Professor of Chemistry and the Faculty Director of the UCSC COSMOS program. His research is focused on the electron-transfer chemistry of functional nanomaterials and their applications in electrochemical energy technologies and microbial control.

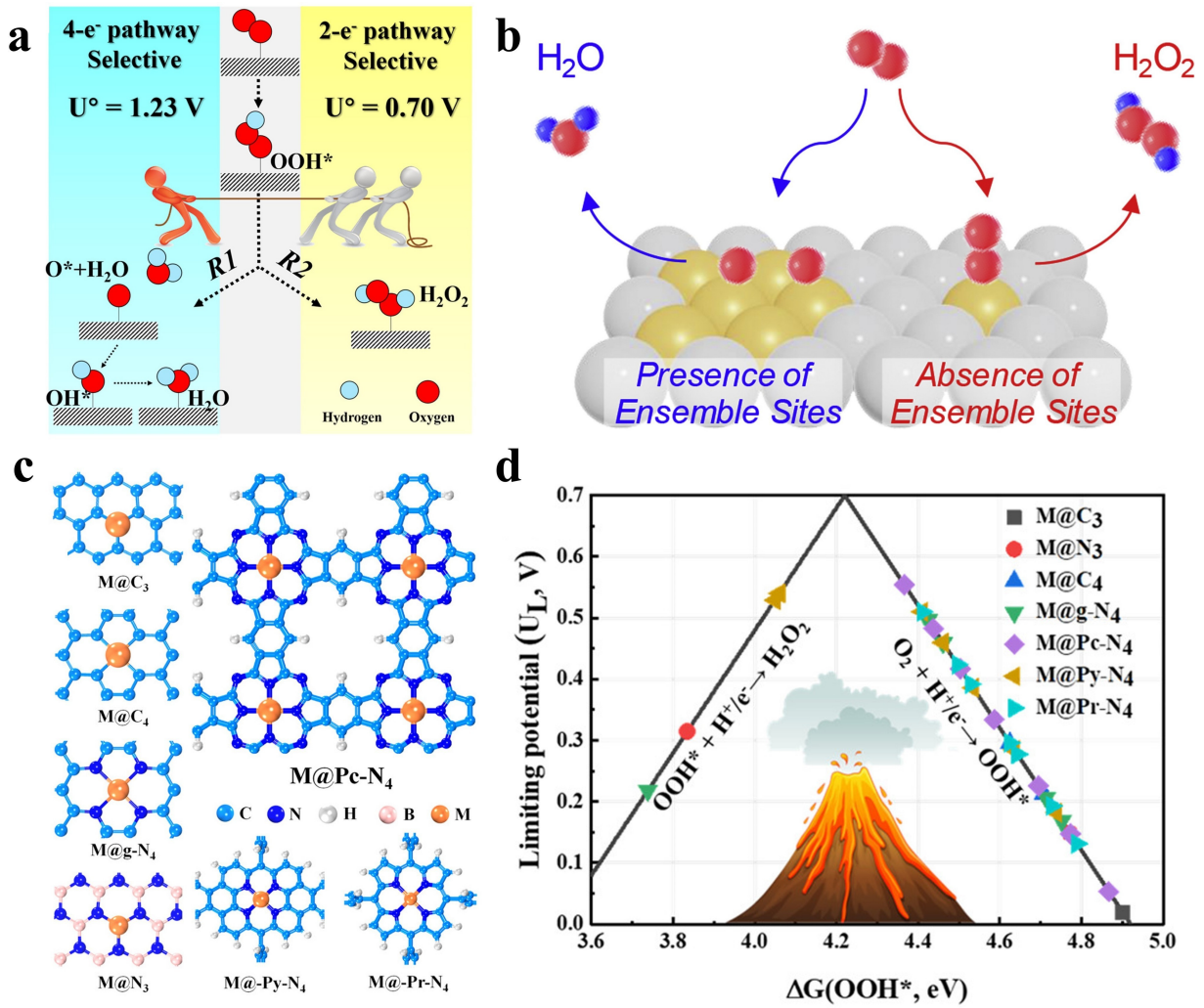

Fig. 1. ORR catalytic process and basic theoretical calculation. (a) Schematic diagram of O_2 electroreduction reaction and equilibrium potential. (b) Effect of ensemble and dispersed metal sites on O_2 adsorption and ORR. (c) Schematic illustrations of various coordination structures of SACs. (d) Volcano relationship between sizable limiting potential (UL) and binding free energy (ΔG_{OOH^*}) for SACs. Panels (a), (c) and (d) reproduced with permission from ref. 36, copyright 2019, the American Chemical Society. Panel (b) Reproduced with permission from ref. 40, copyright 2019, Elsevier.

(Figure 1d). The closer to the top of the volcano, the closer the binding energy to the ideal value for optimal selectivity and activity. They concluded that two factors play a crucial role in the catalytic selectivity of SACs for two-electron ORR. One is the number of d electrons in the metal center. If the central metal atom of SACs is in groups 3 to 10 of the periodic table, increasing the number of d electrons tends to weaken the interaction between the metal active sites and O*, because with the increase of the valence electrons in the d orbitals of the metal sites, the anti-bonding orbitals becomes increasingly occupied by part of the M–O bond below the Fermi level. This is responsible for the reduced stability of the O* intermediates and ultimately enhanced H_2O_2 selectivity. The other key factor is the coordination configuration of the metal atoms, which may impact O* adsorption due to electronic and geometric effects [50,51].

Currently, most SACs reported for H_2O_2 production are prepared by wet chemical methods, such as impregnation and ion exchange [24,52]. Experimentally, mononuclear organometallic complexes are generally used as the precursors and anchored onto the substrate support by select coordination interactions, followed by chemical reduction and/or thermal activation. The strong metal-support interaction is the key to preventing the aggregation of the isolated metal atoms. This can also be aided by a careful control of the loading of the metal precursors.

Below we will highlight recent progress in the design and engineering of SACs, based on both noble and non-noble metals, towards ORR for H_2O_2 production, within the context of the catalyst activity, selectivity and stability.

2 Noble Metal SACs

Noble metal catalysts are the most widely used and successful electrocatalysts for ORR [53,54]. For instance, Pt is well-known for its high electrocatalytic activity in the four-electron reduction of O_2 to H_2O [55]. Many studies have shown that Pt can also effectively catalyze two-electron ORR to produce H_2O_2. Wang et al. [56] proposed that for metal nanoparticles, high H_2O_2 selectivity is achieved only when two conditions are simultaneously met: small metal particle size (less than 5 nm in diameter) and lack of crystalline order. If there is no Pt available at the adjacent site that can break the O–O bond, multi-step reduction of O_2 can not proceed, and H_2O_2 will be the main product [57]. For instance, Song et al. [58] synthesized a Pt SAC on reduced graphene oxide (Pt–SA/rGO) with an ultralow Pt loading of only 0.5 wt %, by using N, N-Dimethylformamide (DMF) as a simple capping agent to realize homogeneous dispersion of Pt atoms under mild conditions. The resulting Pt SACs showed a high activity (3.10 A mg_{Pt}^{-1}) and selectivity (~95 %) towards H_2O_2 production in 0.1M KOH. In another study, Kim et al. [59] developed a general route based on SiO_2 coating to synthesize SACs of various noble metals (i.e., Os, Ru, Rh, Ir and Pt) supported on carbon nanotubes (CNTs) (Figure 2a–c). They first coated CNT with an ionic liquid (IL) containing the metal precursors and annealed the sample at 450 °C. A SiO_2 protective layer was then grown on the surface to immobilize the isolated metal precursors during the thermal activation step. The atomically dispersed noble metal catalysts showed higher selectivity for H_2O_2 production by ORR than their nanoparticle counterparts. It was found that the SACs with weaker oxygen binding were more likely to show better activity towards two-electron ORR, and Rh was situated at the top of the binding energy volcano plot. In fact, Rh SAC exhibited the best activity among the series, but Pt SAC possessed the highest selectivity (Figure 2b) as well as excellent durability, where the activity and selectivity were well retained after 5000 scan cycles in the accelerated degradation test.

Another platinum-group metal, Pd, also has excellent performance in the ORR production of H_2O_2. DFT calculations show that when the single atoms of Pt and Pd were fixed within graphitic carbon nitride (g-C_3N_4) thin layers with carbon black (C@C_3N_4) by taking advantage of the strong coordination of the pyridinic N in g-C_3N_4, O_2 could adsorb onto the surface. Yet the O–O bond length was shorter on the Pd atom (1.31 Å) than that on Pt (1.34 Å) [60]. This implies that Pt is more conducive to the breaking of the O–O bond, has a higher O_2 binding energy (Figure 2d), and is more likely to produce H_2O. Indeed, electrochemically, the C@C_3N_4-0.5 %Pd SAC (Pd content 0.5 %) showed a high ORR activity of 8.5 A mg_{Pd}^{-1}

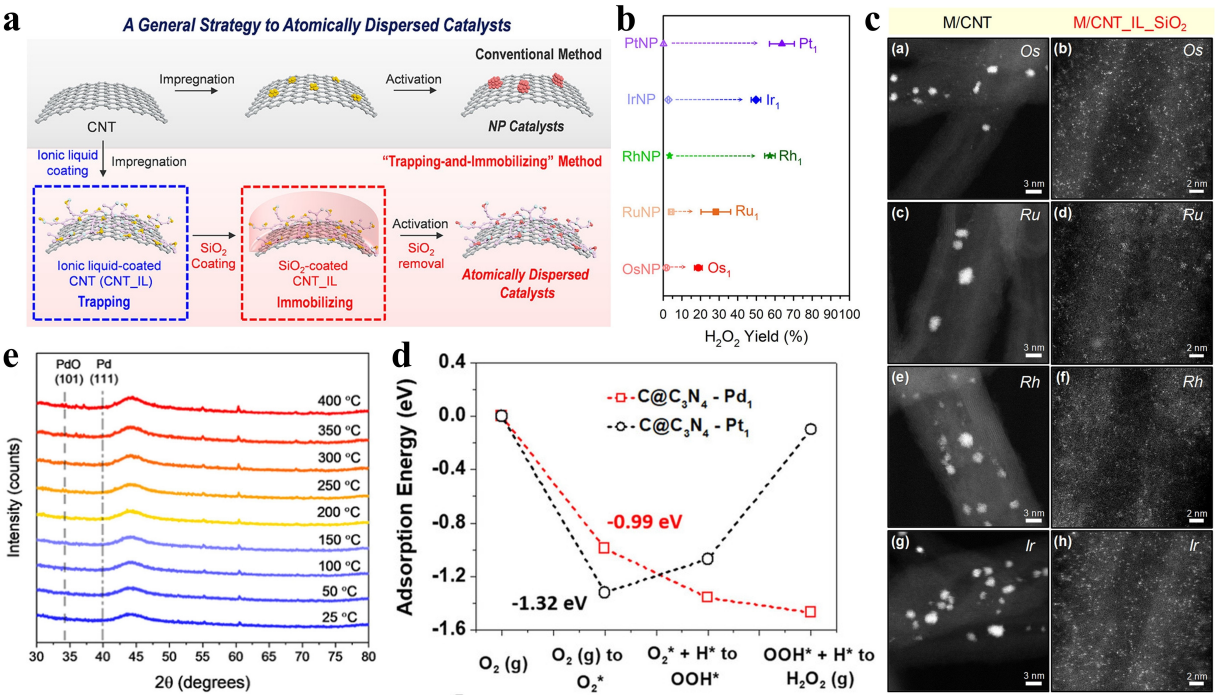

Fig. 2. Synthesis and properties of noble metal SACs. (a) Illustrations of the trapping-and-immobilizing strategy for the preparation of atomically dispersed noble metal catalysts. (b) H_2O_2 yields of five noble metal nanoparticles (NP) and corresponding SACs at $-0.5\ mA\ cm^{-2}$. (c) HAADF-STEM images of various metal NPs (left panels) and SACs (right panels) loaded on CNT. Reproduced with permission from ref. 59, copyright 2020, the American Chemical Society. (d) Energy profile of intermediates adsorbed on atomic Pd and Pt along the ORR pathway at U = 0 V. Reproduced with permission from ref. 60, copyright 2019, the John Wiley and Sons. (e) In situ X-ray diffraction of $PdCl_x$/C SAC at increasing temperatures under a flow of Ar. Reproduced with permission from ref. 61, copyright 2020, the American Chemical Society.

at +0.2 V and high selectivity of up to 94 % for H_2O_2 production in 0.1 M $HClO_4$, much better than that by C@C_3N_4-0.5 %Pt (mass activity less than 1 A mg_{Pt}^{-1}). The onset potentials of the Pd and Pt SACs also varied at +0.67 V and +0.37 V vs RHE, respectively, with an overpotential of 30 mV and 330 mV for the two electron ORR pathway.

Marc et al. [61] also observed high selectivity of Pd SACs in H_2O_2 production. They prepared an atomically dispersed $PdCl_x$/C catalyst (6.7 wt% of Cl, 8.1 wt% of O and 1.3 wt% or 0. 16 at% of Pd) by dropcasting $PdCl_2$ in aqua regia onto the surface of activated carbon and thermal treatment at 140 °C of the dried sample. The C–Cl surface groups were suggested as the anchoring points for the Pd centers, producing bridging Cl species similar to the bulk structure of $PdCl_2$. The selective production of H_2O_2 was found to exceed 90 % and the mass activity was estimated to be 72.8 A g_{Pd}^{-1} in 0.1 M $HClO_4$, a performance significantly better than that of the Pd nanoparticle counterparts (selectivity below 5 %). Electrochemically, the Pd SACs were also found to retain the electrocatalytic activity even after 1000 CV cycles between +0.05 and +0.8 V. Such resistance against electrochemical corrosion was consistent with the chemical stability of the dispersed Pd–Cl species in thermal sintering tests (Figure 2e).

In another study, Cao et al. [54] carried out DFT calculations and *ab initio* molecular dynamics (AIMD) simulations and examined the ORR activity of 25 SACs based on a wide range of transition metals (i.e., Sc to Zn, Y to Cd, Os, Ir, Pt, Au, and Hg) supported on g-C_3N_4. Based on the adsorption free energy of O_2, N-vacancy g-C_3N_4 doped with Pd–Cu hybrid double atoms (PdCu@V_C_3N_4) was found to stand out at the top of the two-electron ORR volcano plot. The activation energy barrier was estimated to be only 0.64 eV for the rate-determining step of the formation of OOH* intermediate, leading to a low overpotential of merely 20 mV. The high activity and selectivity were ascribed to the end-on adsorption of O_2 by the "slope" geometric configuration and electronic interactions of the adjacent hybrid atoms. In such a "slope" structure, the two metal atoms were situated at the top and bottom of the catalyst surface, respectively, providing two adsorption sites for O_2 and H^+ while avoiding O–O bond cleavage by the two metal atoms (Figure 3a). Results from this study suggest that alloying at the single atom scale may be an effective strategy in the

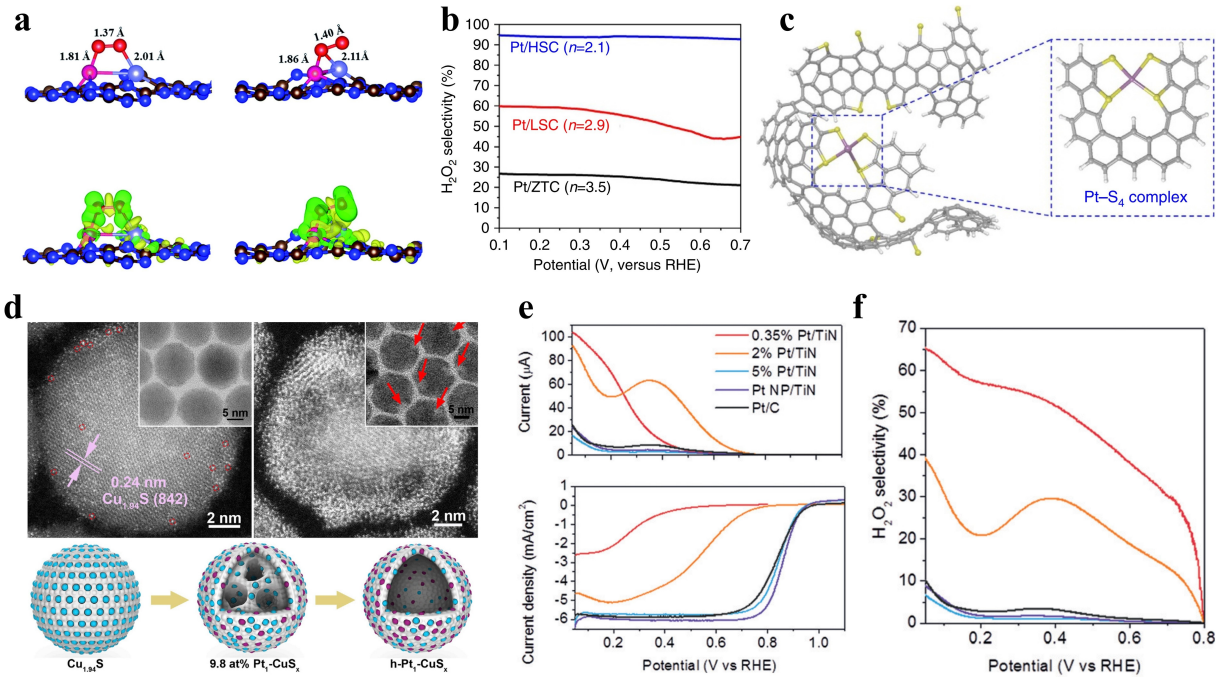

Fig. 3. (a) Optimized structures of O_2 adsorbed on PdCu@V_C_3N_4 in the side-on and end-on configurations. Reproduced with permission from ref. 54, copyright 2020, Royal Society of Chemistry. (b) Selectivity of H_2O_2 production estimated by RRDE experiments of Pt/ZTC, Pt/LSC, and Pt/HSC. (c) Proposed atomistic structure of Pt/HSC with possible thiophene- and thiolate-like functional groups at the graphene edge sites, as well as coordinated Pt species (C: grey, H: white, S: yellow and Pt: purple). Reproduced with permission from ref. 55, copyright 2016, Springer Nature. (d) AC-HAADF-STEM images and TEM images of 0.68 at% and 9.8 at % Pt_1–CuS_x, respectively; and schematic illustration of the structural evolution of h-Pt_1–CuS_x (blue, purple, and white balls represent Cu, Pt, and S atoms, respectively). Insets are the corresponding bright-field images at lower magnification. Reproduced with permission from ref. 62, copyright 2019, Elsevier. (e) ORR ring currents (top panel) and polarization curves (bottom panel) of the Pt/TiN samples at the Pt loadings of 0.35, 2, and 5 wt%. (f) H_2O_2 selectivity calculated from data in (e). Reproduced with permission from ref. 66, copyright 2015, John Wiley and Sons.

design and engineering of high-performance ORR catalysts for selective H_2O_2 production.

The strong affinity of sulphur to transition metals can also be exploited for the preparation of SACs. Choi et al. [55] employed sulphur-containing zeolite-templated carbon (ZTC) to anchor Pt by a conventional wet-impregnation method, followed by H_2 reduction at 250 °C. Three samples were prepared and their ORR activity was evaluated and compared (Figure 3b and 3c). For S-free ZTC, the resulting Pt/ZTC composite contained Pt nanoparticles of ca. 4 nm in diameter. For ZTC with a low S content (4 wt%), Pt clusters (dia. 1–2 nm) were produced in the final example (Pt/LSC); whereas with high S-content ZTC (17 wt%), Pt was embedded into the carbon matrix in the form of PtS_4 (at a high Pt loading of 5 wt%) in the obtained Pt/HSC composite, where no clusters were resolved in high-resolution TEM measurements. Electrochemically, Pt/HSC exhibited an onset potential of ca. +0.71 V for H_2O_2 production in 0.1 M $HClO_4$, close to the thermodynamic potential (eq. 4), and 96 % selectivity. By contrast, the selectivity was markedly lower at only 28 % for Pt/ZTC and 60 % for Pt/LSC. The remarkable performance of Pt/HSC was ascribed to the inactivity of atomically dispersed Pt towards H_2O_2 decomposition. In addition, the Pt/HSC catalysts showed no significant degradation of the electrocatalytic activity, likely because the strong Pt–S interaction.

In another study [62], hollow nanospheres of $Cu_{1.94}S$ with a diameter of 11.4 ± 1.0 nm were used for the embedment of Pt single atoms by reacting with H_2PtCl_6. The resulting Pt_1–CuS_x composites achieved an ultra-high Pt concentration of 24.8 at% (Figure 3d), and in 0.5 M $HClO_4$ effectively reduced O_2 to H_2O_2 with a selectivity of 92 %–96 % in a wide potential range of +0.05 to +0.7 V, much higher than those (10–30 %) for commercial Pt/C, $Cu_{1.94}S$, and PtS_2. The high selectivity and activity were well retained after 10000 CV cycles within the potential range of +0.1 to +0.8 V.

Select metals and metal oxides/nitrides can also be used as effective supporting matrices for the atomic dispersion of catalytic active (metal) atoms. For instance, in an early study [63], when Au nanoparticles were dispersed into a $PdCl_2$ solution, atomic dispersion of Pd into the Au nanoparticles occurred with a Pd content up to 8 %. The resulting Au–Pd alloy exhibited apparent catalytic ability towards two-electron ORR and 95 % selectivity of H_2O_2 production. However, a further increase of the Pd content resulted in the formation of Pd domains and hence a decrease of H_2O_2 selectivity. SACs have also been prepared on metal oxide supports, such as TiO_2 and FeO_x [64,65], by taking advantage of the strong metal-oxygen interactions. Unfortunately, metal oxide supports are usually insulators or semiconductors with low electrical conductivity, and relatively unstable under corrosive electrochemical operating conditions. Therefore, other supports are generally employed. For instance, Yang et al. [66] deposited Pt at various weight percentages onto acid-treated TiN nanoparticles using an incipient wetness impregnation (IWI) method. Experimentally, a H_2PtCl_6 solution was mildly reduced at 100 °C, and Pt centers were embedded at the N vacancies of the TiN support. At the overpotential of −0.05 V, the 0.35 wt% Pt/TiN sample exhibited a mass activity of 78 A g_{Pt}^{-1} for H_2O_2 production in 0.1 M $HClO_4$, with a selectivity up to 90 %. By contrast, at higher Pt loadings where nanoparticles were produced, four-electron ORR was observed instead (Figure 3e and 3f).

From these studies one can see that noble metal SACs are effective ORR catalysts towards the selective production of H_2O_2. High loadings of the SACs can be achieved by coordination with N and S heteroatoms wihin a carbon derivative or embedded within a metal or metal oxide/nitride matrix. The advantage of noble metal-based SACs mainly lies in their strong binding with O_2, and the performance can be readily manipulated by the metal d electrons and coordination configurations of the active sites.

3 Non-noble Metal SACs

Non-noble metal-based SACs have also exhibited apparent ORR activity towards H_2O_2 production. Carbon derivatives are generally used as the supporting matrices [5,16,67–72]. For instance, graphene and carbon nanotubes doped with O, N, F, B, etc have been used rather extensively, into which a range of transition metal atoms (e.g., Co, Ni, Fe, Mn, Cu, etc.) can be embedded, producing stable single-atom catalyst sites [73–75].

Among these, SACs with a M–N–C structure are the most popular [76,77]. Theoretical studies based on DFT calculations [78,79] have shown that the binding free energy of oxygen intermediates on Co–N–C places it near the top of the volcano plot of H_2O_2 production, making it an excellent H_2O_2 catalyst, whereas Mn–N–C and Fe–N–C bind the intermediates too strongly, making them effective H_2O producers instead. However, for Cu–N–C and Ni–N–C catalysts, the overall activities are less well represented by the model, suggesting a minor contribution of the metal centers to the activity, as compared to the N–C defect surroundings (Figure 4a) [37]. Figure 4b shows that the binding energies of OOH*, O*, and OH* are generally proportional to the number of valence electrons in the metal centers from Mn to Cu [80]. That is, the larger the number of metal valence electrons, the weaker the binding of oxygen intermediates to the metal atoms. This is because of the down-shift of the metal d-band center, relative to the Fermi level, that makes it easier to have anti-bonding coupling between the metal d orbital and oxygen 2p orbital. Figure 4c summarizes this phenomenon visually. The experimental results also fully corroborated this trend. At +0.6 V, the Co–N–C catalyst exhibited a kinetic current density of H_2O_2 generation at 1 mA cm^{-2} (equivalent to the mass-normalized current density of 40 A $g_{catalyst}^{-1}$), an onset potential of about +0.7 V, and H_2O_2 Faradaic efficiency over 90 %. In acidic media, the performance was even

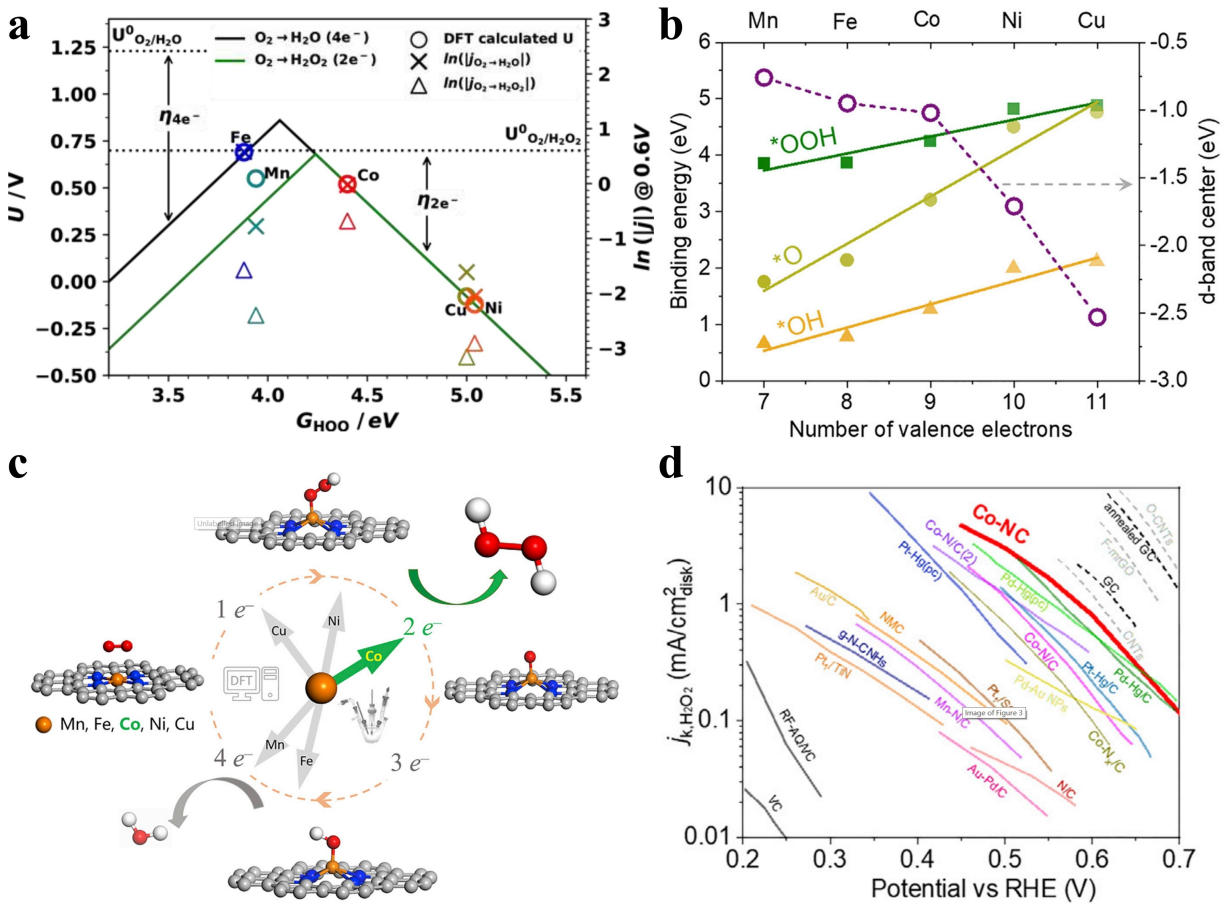

Fig. 4. Theoretical calculation and actual activity of non-noble metal SACs. (a) Thermodynamic relations (volcano plots) for the two- (green solid line) and four-electron ORR (black solid line). Reproduced with permission from ref. 37, copyright 2019, the American Chemical Society. (b) Binding energy (solid symbols) of OOH*, O*, and OH* on M–SAC (M=Mn, Fe, Co, Ni, and Cu) and d-bond center (open circles) of M atom in M–SAC. (c) Schematic of ORR along the two-electron or four-electron pathway on transition-metal SACs anchored in N-doped graphene. (d) Tafel plots of mass-transport corrected current densities for H_2O_2 production in acidic (solid lines) and alkaline media (dashed lines). Reproduced with permission from ref. 80, copyright 2020, Elsevier.

slightly better than the best Pd–Hg alloy catalyst reported previously (Figure 4d).

In the M–N–C SAC systems, the atomic configuration of the MN_x moieties plays a critical role in dictating the ORR activity and selectivity. Suk et al. [81] treated the M–N–C surface with H_2O_2 to incorporate rich oxygen functionalities into the matrix. The formation of C=O and C–O functional groups on the M–N–C catalysts was found to facilitate the two-electron pathway of ORR. Figure 5a shows that the Fe, Mn, and Co SACs all exhibited an increase of the selectivity after H_2O_2 oxidation, but the extent of enhancement varied, Among the series of samples, the oxidized Co–N–C catalyst showed the highest selectivity of more than 85 % in 0.1 M $HClO_4$. They ascribed the boosting of the two-electron ORR pathway by carbon oxidation to weakened oxophilicity at the active MN_xC_y moieties (i.e., electronic effect) and/or pre-occupation of the nearest carbon site by oxygen functionalities (i.e., steric effect).

In another study, Jung et al. [82] studied the change of ORR activity and selectivity of MN_4 sites in more detail. They prepared Co–N–C SACs by mixing and freeze-drying a $CoCl_2 \cdot 6H_2O$ and GO solution, and then pyrolyzed in a tube furnace under an Ar atmosphere. The samples heated at 500 °C and 900 °C are named Co_1–NG (O) and Co_1–NG(R), respectively, and the metal-free one is the comparative sample NG(O). Interestingly, ΔG_{OOH^*} could be adjusted by attaching a functional group near the CoN_4 moiety. For example, when electron-rich species (such as O*) are adsorbed near the CoN_4 portion (Co–N_4 (O)), ΔG_{OOH^*} was found to increase from 3.9 eV to 4.1 eV, very close to the optimal value in the volcano plot (Figure 5b). When two O* were adsorbed near the CoN_4 (Co–N_4(2O)) site, ΔG_{OOH^*} was further increased to 4.5 eV. However, when electron-deficient species such as H^+ were adsorbed near the CoN_4 portion, ΔG_{OOH^*} decreased instead from 3.9 eV to 3.8 eV on Co–N_4(2H), and further to 3.1 eV on Co–N_4(4H). The optimized catalyst Co_1–NG(O) showed a kinetic current density of 2.8 ± 0.2 mA cm^{-2} at +0.7 V and a mass activity at 155 ± 6 A g_{Co}^{-1} in a 0.1 M KOH, with a negligible activity loss

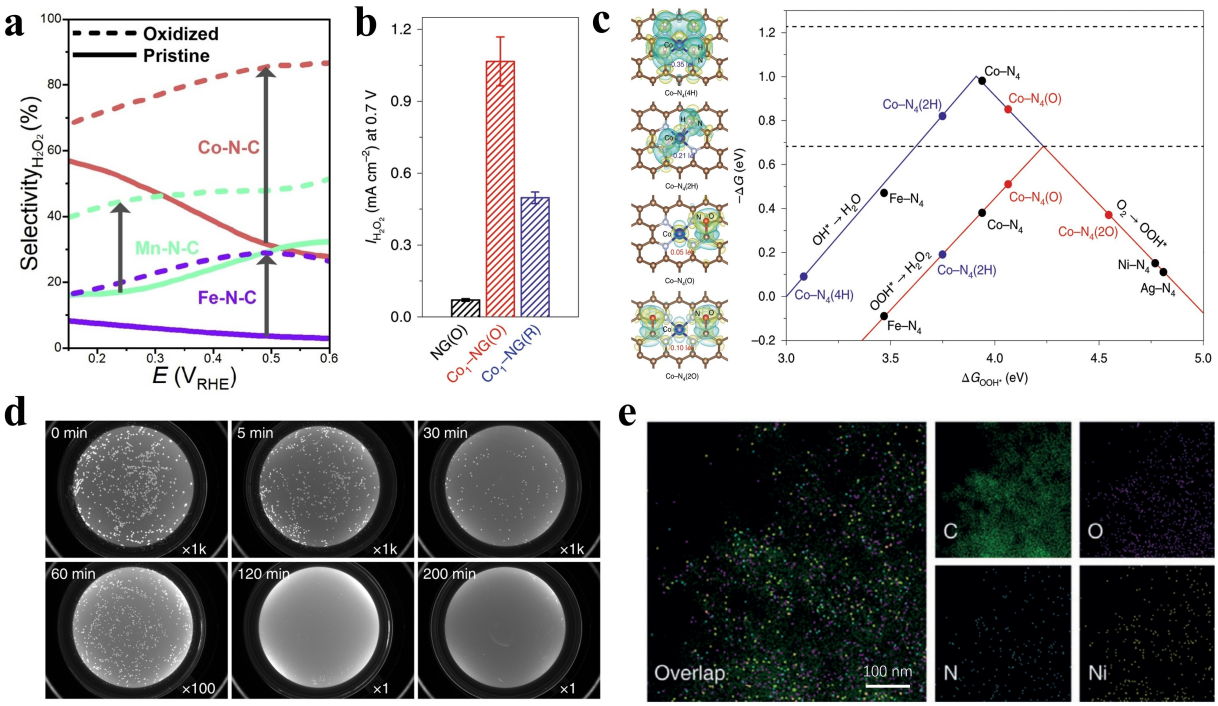

Fig. 5. Performance improvement with M–N–C active sites. (a) Selectivity toward H_2O_2 formation by the M–N–C catalysts before and after H_2O_2 treatment. Reproduced with permission from ref. 81, copyright 2019, Elsevier. (b) Comparison of H_2O_2 current at 0.7 V for NG(O), Co_1–NG(O) and Co_1–NG(R). (c) Differential charge densities of CoN_4/graphene after 4H*, 2H*, O* or 2O* are adsorbed near the cobalt atom and activity volcanoes for the production of H_2O (blue) and H_2O_2 (red) via ORR. Reproduced with permission from ref. 82, copyright 2020, Springer Nature. (d) CCD photographs of overnight cultured plates with spread droplets taken from different time slots during the electrolysis. Reproduced with permission from ref. 85, copyright 2019, Springer Nature. (e) EDS elemental maps of Ni–N_2O_2/C. Reproduced with permission from ref. 87, copyright 2020, John Wiley and Sons.

over 110 h's continuous operation in basic media (Figure 5c).

Interestingly, high-performance ORR catalysts for selective H_2O_2 production can also be obtained by changing the coordination structure of the M–N–C based SACs [83–85]. Jiang et al. [85] found that when the N atom was replaced by O in the Fe–N–C configuration, the OOH* binding at the C position was enhanced. Contrary to the coordination of Fe–C–O, the bonding interaction of C with OOH* in the Fe–N–C system was very weak. They synthesized a series of CNT-supported SACs and examined the effect of the metal centers on the ORR activity by the impregnation and then reduction method, in comparison to the metal-free counterparts that contained only oxygen dopants. Experimentally, metal nitrate was used as the precursor and dispersed on the CNT powder, and the obtained mixture was pyrolyzed in a tube furnace at 600 °C. Among the series, Fe–CNT (Fe loading 0.1 at%) exhibited the best performance towards H_2O_2 generation with a rate of 43 mA cm^{-2} and selectivity of 95.4 % at +0.76 V in 0.1 M KOH. This unique feature could be exploited for water disinfection. From Figure 5d, one can see that Fe–CNT showed a high disinfection efficiency against *E. coli*, inactivating 43 % of the bacterial cells within 5 min and more than 99.9999 % of the bacteria within 120 min.

Graphene-supported Ni SACs have also shown a good performance towards H_2O_2 production. For instance, Song et al. [86] prepared a Ni SAC with Ni–O–C coordination (Ni–SA/G-0) by mixing $NiCl_2$ in DMF with a GO solution, followed by slow $NaBH_4$ reduction in a water/ice bath (Ni loading 1.5 wt%). Extended X-ray absorption fine structure (EXAFS) measurements suggested the absence of a metal-derived crystal structure and Ni was atomically dispersed within the GO matrix by coordinating with four oxygen atoms (NiO_4), in conjunction with results from theoretical calculations. In contrast to the Ni nanoparticle catalyst, Ni–SA/G-0 facilitated the two-electron ORR pathway with a high H_2O_2 selectivity (>94 %) within the potential range of +0.1 to +0.5 V. Remarkably, the mass activity of 2.89 A mg_{Ni}^{-1} at +0.6 V in 0.1 M KOH was significantly better than that (0.51 A mg_{Pt}^{-1}) of commercial Pt/C under the same conditions. Wang et al. [87] prepared a NiN_2O_2 SAC for two-electron ORR by impregnation of a Jacobsen-Ni complex on carbon black, followed by pyrolysis at 300 °C under Ar. The selectivity of H_2O_2 production by NiN_2O_2/C was found to reach a maximum of about 96 % in 0.1 M KOH within the potential range of +0.4 to +0.5 V, in comparison to 68% for carbon alone and 62% for NiN_4/C catalysts (Figure 5e).

For metals such as Mo and Mn, they were rarely mentioned for two-electron ORR. Yet in a recent study [88], Mo SAC with a unique O and S coordination was fabricated at a high Mo loading over 10 wt%, by taking advantage of the combined glucose-chelating and defect-trapping effects. The specific atomic coordination of the resulting Mo_1/OSG–H composite (e.g., M–S_4–C and Mo–O_3S–C) was found to significantly influence the oxygen adsorption behavior and reaction pathway, resulting in a high H_2O_2 selectivity of over 95% in 0.1 M KOH (Figure 6a–c). In another study, Byeon et al. [89] prepared a mesoporous N-doped carbon/manganese hybrid electrocatalyst composed of MnO nanoparticles and MnN_x moieties supported in N-doped carbon (Mn–O/N@NCs) via the silica-assisted polymerization of aniline and subsequent metal impregnation process. The formation of MnO particles (average particle diameter around 200 nm) in the composites effectively mitigated the further reduction of H_2O_2, which is the most frequently encountered issue in electrochemical H_2O_2 production (Figure 6d). A high selectivity (>80 %) in 0.1 M $HClO_4$ and outstanding durability of the Mn–O/N@NCs catalyst was observed.

From these studies, one can see that non-noble metal SACs can also serve as effective ORR catalysts towards the selective production of H_2O_2, with some of the performance even competitive to that of noble metal SACs. These SACs are generally supported on carbon derivatives and used in alkaline media. In the M–N–C systems, the best-performing metal is Co, and two-electron ORR activity can be manipulated by the coordination configuration of the metal centers, similar to the noble metal counterparts.

4 Summary and Perspectives

In summary, SACs have emerged as new, effective ORR catalysts towards the selective electroreduction of oxygen to H_2O_2. Such catalysts can be prepared with both noble metals and non-noble metals embedded in a wide range of supporting matrices, in particular, heteroatom-doped carbon derivatives. Different from traditional nanoparticle catalysts, SACs exhibit the following unique characteristics. First, the isolated atomic sites in SACs can promote the end-on adsorption of O_2 and its intermediates, thus impeding the breaking of the O–O bonds and complete reduction to water. Second, the surface electronic structure can be readily manipulated by the metal-substrate coordination interaction, such that the adsorption energy of important reaction intermediates can be regulated accordingly, a critical step for the optimization of the electrocatalytic activity and selectivity.

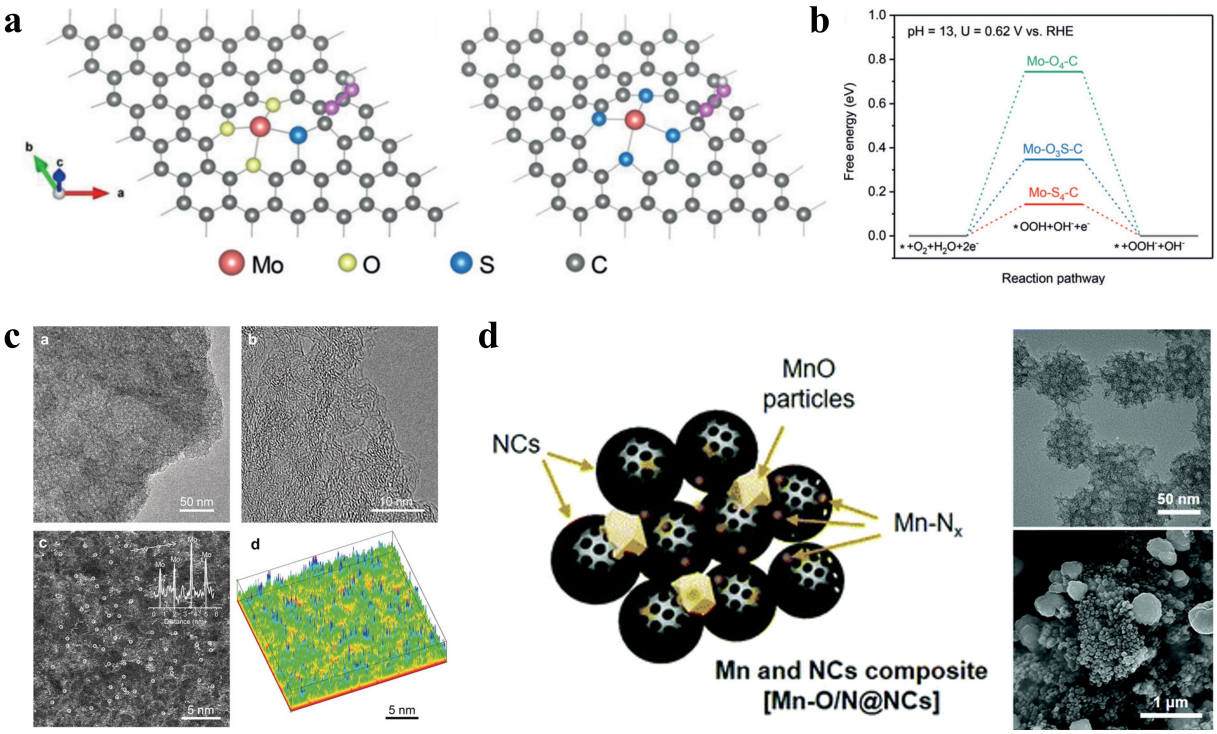

Fig. 6. Non-noble metal SACs and their ORR properties. (a) Atomic configurations of OOH* adsorption on Mo–O_3S–C and Mo–S_4–C. (b) Free energy diagram of two-electron ORR on three substrates under investigation at the equilibrium potential of the reaction. (c) TEM images of Mo_1/OSG–H and pseudo-color surface plot of the HAADF-STEM image. Reproduced with permission from ref. 88, copyright 2020, the American Chemical Society. (d) Schematic illustration of polyaniline-derived N-doped carbon spheres (NCs) and Mn–O/N@NC catalysts (left panel) and TEM of the NCs, SEM images of the Mn–O/N@NC catalyst (right panel). Reproduced with permission from ref. 89, copyright 2020, Royal Society of Chemistry.

Currently, research of SACs has primarily focused on enhanced metal loading and identification of metal centers and coordination configurations, so as to understand the mechanism of SACs and further improve the electrocatalytic performance. Despite substantial progress thus far, critical challenges remain. The main issue lies in the complexity and randomness in the sample structure, as pyrolysis has been the leading method in SAC synthesis. This inevitably produces a discrepancy between the actual materials structures and models used in theoretical calculations and simulations, leading to ambiguity in the identification of the catalytic active sites. In addition, it is known that H_2O_2 is unstable and can readily decompose in alkaline media (especially at pH > 9). However, a large number of SACs, in particular, those based on non-noble metals, are active only in alkaline media. To mitigate these issues, significant breakthroughs on both theoretical and experimental fronts are needed. Specifically, theoretical calculations and simulations will be a powerful tool in the initial screening of potential ORR catalysts, where a range of structural parameters can be evaluated within the context of the ORR pathways and kinetics. Such fundamental insights can then be exploited for the rational design and engineering of high-performance SACs, where development of effective procedures for catalyst preparation is equally important, in particular, to achieve a uniform distribution and coordination of the metal centers. Furthermore, in situ and operando analysis of the ORR catalysts may yield unique insights into the actual atomic sites that are responsible for the ORR activity and selectivity [24]. In fact, research along these lines is ongoing.

Acknowledgment

This work is supported in part by the National Science Foundation (CBET-1848841, CHE-1900235, and CHE-2003685). W.Y.Z. thanks the China Scholarship Council for a research fellowship

Data Availability Statement

All data presented in the present paper are reproduced with permission and available from the publishers listed in the respective figure captions.

References

[1] E. Jung, H. Shin, W. Hooch Antink, Y.-E. Sung, T. Hyeon, *ACS Energy Lett.* **2020**, *5*, 1881–1892.
[2] Y. J. Ko, K. Choi, B. Yang, W. H. Lee, J. Y. Kim, J. W. Choi, K. H. Chae, J. H. Lee, Y. J. Hwang, B. K. Min, H. S. Oh, W. S. Lee, *J. Mater. Chem. A.* **2020**, *8*, 9859–9870.
[3] J. Y. Zhang, H. C. Zhang, M. E. Cheng, Q. Lu, *Small.* **2020**, *16*.
[4] J. Zhou, X. An, H. Lan, H. Liu, J. Qu, *Appl. Surf. Sci.* **2020**, *509*, 144875.
[5] Y. Wu, A. Muthukrishnan, S. Nagata, Y. Nabae, *J. Phys. Chem. C.* **2019**, *123*, 4590–4596.
[6] K. Yuan, D. Lützenkirchen-Hecht, L. Li, L. Shuai, Y. Li, R. Cao, M. Qiu, X. Zhuang, M. K. H. Leung, Y. Chen, U. Scherf, *J. Am. Chem. Soc.* **2020**, *142*, 2404–2412.
[7] Y. Y. Jiang, P. J. Ni, C. X. Chen, Y. Z. Lu, P. Yang, B. Kong, A. Fisher, X. Wang, *Adv. Energy Mater.* **2018**, *8*, 1801909.
[8] H. He, B. Jiang, J. Yuan, Y. Liu, X. Bi, S. Xin, *J. Colloid Interface Sci.* **2019**, *533*, 471–480.
[9] Y. Cao, G. Zhou, X. Chen, Q. Qiao, C. Zhao, X. Sun, X. Zhong, G. Zhuang, S. Deng, Z. Wei, Z. Yao, L. Huang, J. Wang, *J. Mater. Chem. A.* **2020**, *8*, 124–137.
[10] T. He, B. Lu, Y. Chen, Y. Wang, Y. Zhang, J. L. Davenport, A. P. Chen, C.-W. Pao, M. Liu, Z. Sun, A. Stram, A. Mordaunt, J. Velasco, Y. Ping, Y. Zhang, S. Chen, *Research.* **2019**, *2019*, 6813585.
[11] Q. Liu, Q. Li, S. Chen, *Curr. Opin. Electrochem.* **2020**, *21*, 46–54.
[12] S. Y. Park, H. Abroshan, X. Shi, H. S. Jung, S. Siahrostami, X. Zheng, *ACS Energy Lett.* **2019**, *4*, 352–357.
[13] V. Viswanathan, H. A. Hansen, J. K. Nørskov, *J. Phys. Chem. Lett.* **2015**, *6*, 4224–4228.
[14] C. Ponce de León, *Nat. Can.* **2020**, *3*, 96–97.
[15] C. Xia, S. Back, S. Ringe, K. Jiang, F. Chen, X. Sun, S. Siahrostami, K. Chan, H. Wang, *Nat. Can.* **2020**, *3*, 125–134.
[16] H. W. Kim, V. J. Bukas, H. Park, S. Park, K. M. Diederichsen, J. Lim, Y. H. Cho, J. Kim, W. Kim, T. H. Han, J. Voss, A. C. Luntz, B. D. McCloskey, *ACS Catal.* **2020**, *10*, 852–863.
[17] V. Čolić, S. Yang, Z. Révay, I. E. L. Stephens, I. Chorkendorff, *Electrochim. Acta.* **2018**, *272*, 192–202.
[18] K. Jiang, J. Zhao, H. Wang, *Adv. Funct. Mater.* **2020**, 2003321.
[19] D. San Roman, D. Krishnamurthy, R. Garg, H. Hafiz, M. Lamparski, N. T. Nuhfer, V. Meunier, V. Viswanathan, T. Cohen-Karni, *ACS Catal.* **2020**, *10*, 1993–2008.
[20] N. Wang, S. Ma, J. Duan, X. Zhai, F. Guan, X. Wang, B. Hou, *Electrochim. Acta.* **2020**, *340*, 135880.
[21] S. Chen, Z. Chen, S. Siahrostami, D. Higgins, D. Nordlund, D. Sokaras, T. R. Kim, Y. Liu, X. Yan, E. Nilsson, R. Sinclair, J. K. Nørskov, T. F. Jaramillo, Z. Bao, *J. Am. Chem. Soc.* **2018**, *140*, 7851–7859.
[22] L. Zhang, J. M. T. A. Fischer, Y. Jia, X. Yan, W. Xu, X. Wang, J. Chen, D. Yang, H. Liu, L. Zhuang, M. Hankel, D. J. Searles, K. Huang, S. Feng, C. L. Brown, X. Yao, *J. Am. Chem. Soc.* **2018**, *140*, 10757–10763.
[23] Y. Lu, Y. Jiang, X. Gao, W. Chen, *Chem. Commun.* **2014**, *50*, 8464–8467.
[24] B. Lu, Q. Liu, S. Chen, *ACS Catal.* **2020**, *10*, 7584–7618.
[25] Y. Peng, B. Lu, S. Chen, *Adv. Mater.* **2018**, *30*, 1801995.
[26] H. Xu, D. Cheng, D. Cao, X. C. Zeng, *Nat. Can.* **2018**, *1*, 339–348.
[27] A. Wang, J. Li, T. Zhang, *Nat. Rev. Chem.* **2018**, *2*, 65–81.
[28] H. Li, H. Zhu, Z. Zhuang, S. Lu, F. Duan, M. Du, *Sustain. Energy. Fuels.* **2020**, *4*, 996–1011.
[29] Y. Pan, C. Zhang, Z. Liu, C. Chen, Y. Li, *Matter.* **2020**, *2*, 78–110.
[30] M. Fan, J. Cui, J. Wu, R. Vajtai, D. Sun, P. M. Ajayan, *Small.* **2020**, *16*, 1906782.
[31] X. Li, S. Duan, E. Sharman, Y. Zhao, L. Yang, Z. Zhuo, P. Cui, J. Jiang, Y. Luo, *J. Mater. Chem. A.* **2020**, *8*, 10193–10198.
[32] P. Hu, K. Liu, C. P. Deming, S. Chen, *J. Chem. Technol. Biotechnol.* **2015**, *90*, 2132–2151.
[33] W. Niu, L. Li, S. Chen, *J. Electrochem.* **2017**, *23*, 110.

[34] Y. Peng, B. Lu, N. Wang, J. E. Lu, C. Li, Y. Ping, S. Chen, *ACS Appl. Mater. Interfaces.* **2019**, *11*, 24707–24714.
[35] Q. Liu, Y. Peng, Q. Li, T. He, D. Morris, F. Nichols, R. Mercado, P. Zhang, S. Chen, *ACS Appl. Mater. Interfaces.* **2020**, *12*, 17641–17650.
[36] X. Guo, S. Lin, J. Gu, S. Zhang, Z. Chen, S. Huang, *ACS Catal.* **2019**, *9*, 11042–11054.
[37] Y. Sun, L. Silvioli, N. R. Sahraie, W. Ju, J. Li, A. Zitolo, S. Li, A. Bagger, L. Arnarson, X. Wang, T. Moeller, D. Bernsmeier, J. Rossmeisl, F. Jaouen, P. Strasser, *J. Am. Chem. Soc.* **2019**, *141*, 12372–12381.
[38] Q. Gao, *Ionics.* **2020**, *26*, 2453–2465.
[39] Y. Jia, X. D. Yao, *Chem.* **2020**, *6*, 548–550.
[40] J. H. Kim, Y.-T. Kim, S. H. Joo, *Curr. Opin. Electrochem.* **2020**, *21*, 109–116.
[41] M. A. Hunter, J. M. T. A. Fischer, Q. Yuan, M. Hankel, D. J. Searles, *ACS Catal.* **2019**, *9*, 7660–7667.
[42] A. Verdaguer-Casadevall, D. Deiana, M. Karamad, S. Siahrostami, P. Malacrida, T. W. Hansen, J. Rossmeisl, I. Chorkendorff, I. E. L. Stephens, *Nano Lett.* **2014**, *14*, 1603–1608.
[43] Y. Xiao, W. Zhang, *Electrocatalysis.* **2020**, *11*, 393–404.
[44] S. Siahrostami, A. Verdaguer-Casadevall, M. Karamad, D. Deiana, P. Malacrida, B. Wickman, M. Escudero-Escribano, E. A. Paoli, R. Frydendal, T. W. Hansen, I. Chorkendorff, I. E. L. Stephens, J. Rossmeisl, *Nat. Mater.* **2013**, *12*, 1137–1143.
[45] C. Deng, R. He, W. Shen, M. Li, *Phys. Chem. Chem. Phys.* **2019**, *21*, 18589–18594.
[46] S. C. Perry, D. Pangotra, L. Vieira, L. I. Csepei, V. Sieber, L. Wang, C. P. de Leon, F. C. Walsh, *Nat. Rev. Chem.* **2019**, *3*, 442–458.
[47] T. Wang, Z. Zeng, L. Cao, Z. Li, X. Hu, B. An, C. Wang, W. Lin, *Chem. Eur. J.* **2018**, *24*, 17011–17018.
[48] Y.-H. Wang, Z. K. Goldsmith, P. E. Schneider, C. W. Anson, J. B. Gerken, S. Ghosh, S. Hammes-Schiffer, S. S. Stahl, *J. Am. Chem. Soc.* **2018**, *140*, 10890–10899.
[49] Y.-H. Wang, M. L. Pegis, J. M. Mayer, S. S. Stahl, *J. Am. Chem. Soc.* **2017**, *139*, 16458–16461.
[50] L. Wu, S. Hu, W. Yu, S. Shen, T. Li, *NPJ. Comput. Mater.* **2020**, *6*, 23.
[51] A. Bruix, Y. Lykhach, I. Matolínová, A. Neitzel, T. Skála, N. Tsud, M. Vorokhta, V. Stetsovych, K. Ševčíková, J. Mysliveček, R. Fiala, M. Václavů, K. C. Prince, S. Bruyère, V. Potin, F. Illas, V. Matolín, J. Libuda, K. M. Neyman, *Angew. Chem. Int. Ed.* **2014**, *53*, 10525–10530.
[52] J. Liu, *ACS Catal.* **2017**, *7*, 34–59.
[53] B. Garlyyev, J. Fichtner, O. Pique, O. Schneider, A. S. Bandarenka, F. Calle-Vallejo, *Chem. Sci.* **2019**, *10*, 8060–8075.
[54] Y. Cao, C. Zhao, Q. Fang, X. Zhong, G. Zhuang, S. Deng, Z. Wei, Z. Yao, J. Wang, *J. Mater. Chem. A.* **2020**, *8*, 2672–2683.
[55] C. H. Choi, M. Kim, H. C. Kwon, S. J. Cho, S. Yun, H.-T. Kim, K. J. J. Mayrhofer, H. Kim, M. Choi, *Nat. Commun.* **2016**, *7*, 10922.
[56] Y. L. Wang, S. Gurses, N. Felvey, A. Boubnov, S. S. Mao, C. X. Kronawitter, *ACS Catal.* **2019**, *9*, 8453–8463.
[57] C. H. Choi, H. C. Kwon, S. Yook, H. Shin, H. Kim, M. Choi, *J. Phys. Chem. C.* **2014**, *118*, 30063–30070.
[58] X. Song, N. Li, H. Zhang, H. Wang, L. Wang, Z. Bian, *J. Power Sources.* **2019**, *435*, 226771.
[59] J. H. Kim, D. Shin, J. Lee, D. S. Baek, T. J. Shin, Y.-T. Kim, H. Y. Jeong, J. H. Kwak, H. Kim, S. H. Joo, *ACS Nano.* **2020**, *14*, 1990–2001.
[60] H.-E. Kim, I. H. Lee, J. Cho, S. Shin, H. C. Ham, J. Y. Kim, H. Lee, *ChemElectroChem.* **2019**, *6*, 4757–4764.
[61] M. Ledendecker, E. Pizzutilo, G. Malta, G. V. Fortunato, K. J. J. Mayrhofer, G. J. Hutchings, S. J. Freakley, *ACS Catal.* **2020**, *10*, 5928–5938.
[62] R. Shen, W. Chen, Q. Peng, S. Lu, L. Zheng, X. Cao, Y. Wang, W. Zhu, J. Zhang, Z. Zhuang, C. Chen, D. Wang, Y. Li, *Chem.* **2019**, *5*, 2099–2110.
[63] J. S. Jirkovský, I. Panas, E. Ahlberg, M. Halasa, S. Romani, D. J. Schiffrin, *J. Am. Chem. Soc.* **2011**, *133*, 19432–19441.
[64] C. Chu, D. Huang, Q. Zhu, E. Stavitski, J. A. Spies, Z. Pan, J. Mao, H. L. Xin, C. A. Schmuttenmaer, S. Hu, J.-H. Kim, *ACS Catal.* **2019**, *9*, 626–631.
[65] H. Song, L. Wei, C. Chen, C. Wen, F. Han, *J. Catal.* **2019**, *376*, 198–208.
[66] S. Yang, J. Kim, Y. J. Tak, A. Soon, H. Lee, *Angew. Chem. Int. Ed.* **2016**, *55*, 2058–2062.
[67] J. Park, Y. Nabae, T. Hayakawa, M.-a. Kakimoto, *ACS Catal.* **2014**, *4*, 3749–3754.
[68] S. Chen, Z. Chen, S. Siahrostami, T. R. Kim, D. Nordlund, D. Sokaras, S. Nowak, J. W. F. To, D. Higgins, R. Sinclair, J. K. Nørskov, T. F. Jaramillo, Z. Bao, *ACS Sustainable Chem. Eng.* **2018**, *6*, 311–317.
[69] N. Jia, T. Yang, S. Shi, X. Chen, Z. An, Y. Chen, S. Yin, P. Chen, *ACS Sustainable Chem. Eng.* **2020**, *8*, 2883–2891.
[70] L. Zhang, L. Li, H. Chen, Z. Wie, *Chem. Eur. J.* **2020**, *26*, 3973–3990.
[71] P. Zhang, J.-S. Wei, X.-B. Chen, H.-M. Xiong, *J. Colloid Interface Sci.* **2019**, *537*, 716–724.
[72] Z. Lu, G. Chen, S. Siahrostami, Z. Chen, K. Liu, J. Xie, L. Liao, T. Wu, D. Lin, Y. Liu, T. F. Jaramillo, J. K. Nørskov, Y. Cui, *Nat. Can.* **2018**, *1*, 156–162.
[73] S. Kattel, G. Wang, *J. Mater. Chem. A.* **2013**, *1*, 10790–10797.
[74] Y. Yang, H. Zhang, Z. Liang, Y. Yin, B. Mei, F. Song, F. Sun, S. Gu, Z. Jiang, Y. Wu, Z. Zhu, *J. Energy Chem.* **2020**, *44*, 131–137.
[75] Y. Zhou, W. Yang, W. Utetiwabo, Y.-m. Lian, X. Yin, L. Zhou, P. Yu, R. Chen, S. Sun, *J. Phys. Chem. Lett.* **2020**, *11*, 1404–1410.
[76] H. Fei, J. Dong, Y. Feng, C. S. Allen, C. Wan, B. Volosskiy, M. Li, Z. Zhao, Y. Wang, H. Sun, P. An, W. Chen, Z. Guo, C. Lee, D. Chen, I. Shakir, M. Liu, T. Hu, Y. Li, A. I. Kirkland, X. Duan, Y. Huang, *Nat. Can.* **2018**, *1*, 63–72.
[77] M. Campos, W. Siriwatcharapiboon, R. J. Potter, S. L. Horswell, *Catal. Today.* **2013**, *202*, 135–143.
[78] R. Hu, Y. Li, Q. Zeng, J. Shang, *Appl. Surf. Sci.* **2020**, *525*, 146588.
[79] Y. Yang, W. Qi, J. Niu, F. Chen, W. Li, *Int. J. Hydrogen Energy.* **2020**, *45*, 15465–15475.
[80] J. Gao, H. b Yang, X. Huang, S.-F. Hung, W. Cai, C. Jia, S. Miao, H. M. Chen, X. Yang, Y. Huang, T. Zhang, B. Liu, *Chem.* **2020**, *6*, 658–674.
[81] M. Suk, M. W. Chung, M. H. Han, H.-S. Oh, C. H. Choi, *Catal. Today.* **2019**, in press.
[82] E. Jung, H. Shin, B.-H. Lee, V. Efremov, S. Lee, H. S. Lee, J. Kim, W. Hooch Antink, S. Park, K.-S. Lee, S.-P. Cho, J. S. Yoo, Y.-E. Sung, T. Hyeon, *Nat. Mater.* **2020**, *19*, 436–442.
[83] H. Cao, G.-J. Xia, J.-W. Chen, H.-M. Yan, Z. Huang, Y.-G. Wang, *J. Phys. Chem. C.* **2020**, *124*, 7287–7294.
[84] S. L. Hooe, C. W. Machan, *J. Am. Chem. Soc.* **2019**, *141*, 4379–4387.
[85] K. Jiang, S. Back, A. J. Akey, C. Xia, Y. Hu, W. Liang, D. Schaak, E. Stavitski, J. K. Nørskov, S. Siahrostami, H. Wang, *Nat. Commun.* **2019**, *10*, 3997.

[86] X. Song, N. Li, H. Zhang, L. Wang, Y. Yan, H. Wang, L. Wang, Z. Bian, *ACS Appl. Mater. Interfaces.* **2020**, *12*, 17519–17527.
[87] Y. Wang, R. Shi, L. Shang, G. I. N. Waterhouse, J. Zhao, Q. Zhang, L. Gu, T. Zhang, *Angew. Chem. Int. Ed.* **2020**, in press.
[88] C. Tang, Y. Jiao, B. Shi, J.-N. Liu, Z. Xie, X. Chen, Q. Zhang, S.-Z. Qiao, *Angew. Chem. Int. Ed.* **2020**, *59*, 9171–9176.
[89] A. Byeon, J. Cho, J. M. Kim, K. H. Chae, H.-Y. Park, S. W. Hong, H. C. Ham, S. W. Lee, K. R. Yoon, J. Y. Kim, *Nanoscale Horiz.* **2020**, *5*, 832–838.

Received: July 13, 2020
Accepted: August 17, 2020
Published online on September 8, 2020

